On the permeation of large organic cations through the pore of ATP-gated P2X receptors

Mahboubi Harkat[a,b,1], Laurie Peverini[a,b,1], Adrien H. Cerdan[b,c], Kate Dunning[a,b], Juline Beudez[a,b], Adeline Martz[a,b], Nicolas Calimet[b,c], Alexandre Specht[a,b], Marco Cecchini[b,c], Thierry Chataigneau[a,b], and Thomas Grutter[a,b,2]

[a]Laboratoire de Conception et Application de Molécules Bioactives, Équipe de Chimie et Neurobiologie Moléculaire, Faculté de Pharmacie, Centre National de la Recherche Scientifique (CNRS), UMR 7199, F-67400 Illkirch, France; [b]Université de Strasbourg, F-67000 Strasbourg, France; and [c]Laboratoire d'Ingénierie des Fonctions Moléculaires, Institut de Science et d'Ingénierie Supramoléculaires (ISIS), UMR 7006, CNRS, F-67000 Strasbourg, France

Edited by Christopher Miller, Howard Hughes Medical Institute, Brandeis University, Waltham, MA, and approved March 31, 2017 (received for review January 25, 2017)

Pore dilation is thought to be a hallmark of purinergic P2X receptors. The most commonly held view of this unusual process posits that under prolonged ATP exposure the ion pore expands in a striking manner from an initial small-cation conductive state to a dilated state, which allows the passage of larger synthetic cations, such as *N*-methyl-D-glucamine ($NMDG^+$). However, this mechanism is controversial, and the identity of the natural large permeating cations remains elusive. Here, we provide evidence that, contrary to the time-dependent pore dilation model, ATP binding opens an $NMDG^+$-permeable channel within milliseconds, with a conductance that remains stable over time. We show that the time course of $NMDG^+$ permeability superimposes that of Na^+ and demonstrate that the molecular motions leading to the permeation of $NMDG^+$ are very similar to those that drive Na^+ flow. We found, however, that $NMDG^+$ "percolates" 10 times slower than Na^+ in the open state, likely due to a conformational and orientational selection of permeating molecules. We further uncover that several P2X receptors, including those able to desensitize, are permeable not only to $NMDG^+$ but also to spermidine, a large natural cation involved in ion channel modulation, revealing a previously unrecognized P2X-mediated signaling. Altogether, our data do not support a time-dependent dilation of the pore on its own but rather reveal that the open pore of P2X receptors is wide enough to allow the permeation of large organic cations, including natural ones. This permeation mechanism has considerable physiological significance.

pore dilation | purinergic receptor | photoswitches | YO-PRO uptake | spermidine

P2X receptors are nonselective cation channels activated by adenosine 5′-triphosphate (ATP). They are integral membrane proteins and form a family of trimeric receptors composed of seven subunits (P2X1–P2X7) that are involved in a wide range of physiological and pathological processes, including pain sensation, hearing protection, taste, modulation of neurotransmitter release, hypertension, inflammation, and neuropathic pain (1–5). P2X receptors have, therefore, attracted attention as promising therapeutic targets (5, 6). Supported by recent X-ray structures (7–11), a functional receptor is composed of three subunits that assemble in the cell membrane as a homo- or heterotrimer to form a central transmembrane pore (12, 13). Each subunit comprises two transmembrane helices, named TM1 and TM2, which are linked by an extracellular domain, where the ATP-binding sites are nestled. In response to a short application of ATP, the pore rapidly opens on the millisecond timescale—a process known as gating—to a state that is selective to small inorganic cations, such as Na^+, K^+, and Ca^{2+} ions. The flow of these cations is estimated to occur at relatively high conduction rates, from 6 to 20 × 10^6 ions per second at a given driving force amplitude (14–16). This rapidly affects the ion balance of the cell and consequently initiates signal transduction. This open state is sometimes referred to as I_1 state (2).

A remarkable feature of P2X receptors is that a longer ATP application causes a striking time-dependent pore dilation of the channel. This process, named pore dilation, is observed only for selected subtypes, notably homomeric P2X2, P2X4, and P2X7 and heteromeric receptors P2X2/3 and P2X2/5 (17–21). Different possible mechanisms have been proposed to explain pore dilation (22, 23), but the most prevailing one posits that the open pore of the initial I_1 state progressively dilates for several seconds to form an enlarged pore, denoted I_2 state, that is permeable to large organic cations such as *N*-methyl-D-glucamine ($NMDG^+$) or fluorescent dyes such as ethidium bromide and YO-PRO-1, a carbocyanine DNA binding dye (2). As these cations are larger than small inorganic ions, they are believed to be impermeable to the I_1 state. This belief has been supported by many biophysical studies, including atomic force microscopy (AFM), patch-clamp electrophysiology, fluorescent dye uptakes, and real-time conformational change measurements (17, 18, 24–31). However, the molecular mechanism of pore expansion is still unclear.

Very recently, a study has challenged the pore dilation paradigm (32). The study suggests that the slow transition toward the I_2 state is not caused by a progressive change in the permeability ratio of $NMDG^+$ relative to Na^+, which is usually determined by measuring the hallmark shift in equilibrium potentials by patch-clamp electrophysiology under bi-ionic conditions but rather by a dramatic, unappreciated change of the concentrations of these ions inside the cell. Moreover, this study showed that $NMDG^+$ permeability is rapidly activated and can be inhibited when a

Significance

Unlike many ion channels whose pore conductances remain relatively stable over time, it is thought that prolonged ATP applications to P2X receptors cause a striking increase over time in the permeability of large molecules, a process dubbed pore dilation. However, this mechanism remains poorly understood and highly controversial. Here, we use different methods spanning single-channel recordings, photochemistry, molecular biology, and computations to show that contrary to longstanding view, rapid activation by ATP allows the stable passage of large cations through the P2X pore. We further discover that spermidine, a large natural cation known to modulate other ion channels, is able to transit through many P2X receptors, including those thought to be nondilating. Our data thus reveal an unacknowledged P2X-mediated signaling.

Author contributions: A.S., M.C., and T.G. designed research; M.H., L.P., A.H.C., K.D., J.B., A.M., N.C., A.S., M.C., and T.C. performed research; M.H., L.P., A.H.C., K.D., J.B., A.M., N.C., A.S., M.C., T.C., and T.G. analyzed data; and T.G. wrote the paper.

The authors declare no conflict of interest.

This article is a PNAS Direct Submission.

[1]M.H. and L.P. contributed equally to this work.

[2]To whom correspondence should be addressed. Email: grutter@unistra.fr.

This article contains supporting information online at www.pnas.org/lookup/suppl/doi:10.1073/pnas.1701379114/-/DCSupplemental.

pore-lining cysteine residue is reacted with methanethiosulfonate (MTS) reagents, suggesting that the open state of P2X receptors exhibits measurable and stable permeability to large cations. In line with this work, pore dilation has never been observed at the single-channel level (16, 33), and no crystal structure of a dilated state has been reported to date, making the study of this peculiar state particularly difficult. Finally, the physiological relevance of P2X pore dilation remains unclear, especially due to the unknown identity of the natural molecules that permeate through the dilated state. A recent work has, however, shown that genetically determined P2X7 dilated pore formation regulates variability in chronic pain sensitivity (34). The study revealed that in women having undergone a mastectomy there is a genetic association between lower pain intensity and the hypofunctional His270 (rs7958311) allele of *P2RX7* gene, suggesting that selectively targeting P2X pore formation may be a new strategy for individualizing the treatment of chronic pain. The concept of pore dilation of P2X receptors has remained a matter of controversy for almost 20 years, and as such, understanding of this molecular mechanism with new approaches represents a challenging and pertinent issue.

In this paper, we discover the molecular mechanism of permeation of large organic cations in P2X receptors. Contrary to the prevailing assumptions, we provide evidence by single-channel recordings that the pore does not undergo a time-dependent dilation upon opening but rather enters rapidly, in response to ATP binding, a state that allows the stable passage of large organic cations. In addition, we designed and used photo-switchable cross-linkers of different lengths to probe conformational changes of engineered cysteine-substituted P2X2 receptors that are associated with $NMDG^+$ and YO-PRO-1 permeability. We demonstrate that the molecular motions leading to the permeation of these large organic cations are very similar to those that drive Na^+ flow. We further reveal by molecular dynamics (MD) simulations a complex mechanism for $NMDG^+$ permeation, which involves both a conformational and orientational selection of the permeating molecules. Finally, we uncover that desensitizing P2X receptors have the capacity to transiently conduct $NMDG^+$ ions in response to ATP binding and identify spermidine as a natural large molecule able to permeate selected human P2X pores. Our results underscore a previously unappreciated P2X signaling.

Results

ATP Gates a Pore That Is Immediately Permeable to $NMDG^+$. In a recent study carried out in P2X2 receptors, it has been shown that ATP rapidly gates macroscopic currents in symmetric $NMDG^+$ solutions (32). To determine whether this occurs at the level of the single channel, we used the outside-out configuration of the patch-clamp technique that enables fast solution exchange at the cell membrane on the millisecond time scale. We used symmetric $NMDG^+$ solutions, in which $NMDG^+$ is present in both the external (outside) and internal (inside the pipette) solutions ($NMDG^+_{out}/NMDG^+_{in}$) and thus represents the only carrier of cationic currents. To increase seal resistance and patch stability, fluoride ions (F^-) were used as internal counterions to $NMDG^+$ cations (*Materials and Methods*). We transiently transfected human embryonic kidney (HEK-293) cells with plasmids encoding the rat P2X2–3T, which is a cysteine-less mutated receptor that retains wild-type P2X2 functionality (35) but displays increased single-channel conductance (36). In a first series of experiments, we used excised outside-out patches that contained multiple channels and observed robust inward $NMDG^+$ currents that developed rapidly following fast perfusion of 3 μM ATP, while holding the voltage to –120 mV (activation time constant $\tau_{NMDG+} = 203 \pm 47$ ms, $n = 9$ patches; Fig. 1*A*, *Left* and Fig. S1 *A* and *B*). $NMDG^+$ currents remained constant during the 6-s time

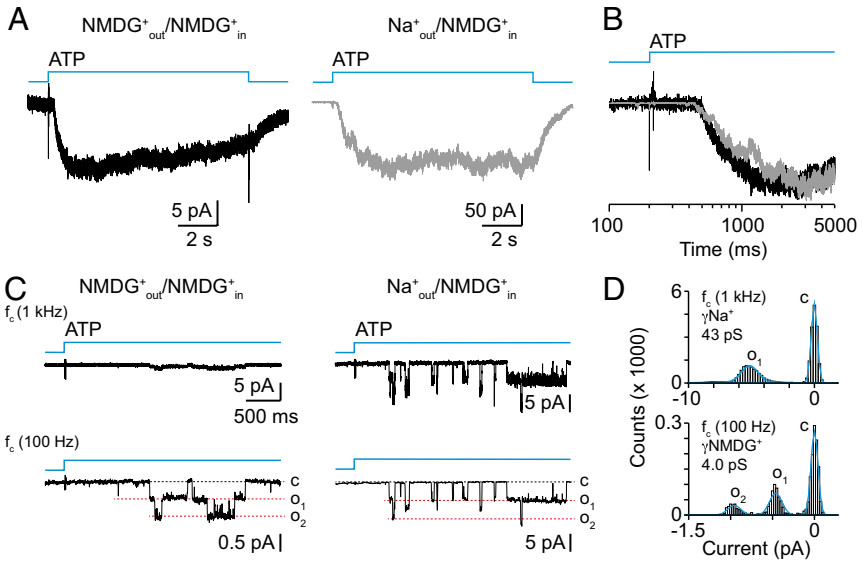

Fig. 1. Rapid ATP activation of P2X2–3T receptors induces instantaneous and stable permeation of $NMDG^+$. (*A*) Fast application of ATP (3 μM, blue traces) to a multiple channel-containing outside-out patch from HEK-293 cells expressing the P2X2–3T receptor evokes rapid $NMDG^+$ (*Left*) and Na^+ (*Right*) currents recorded at –120 mV. The patch was first bathed in extracellular $NMDG^+$ solution ($NMDG^+_{out}/NMDG^+_{in}$, *Left*) and then rapidly exchanged to extracellular Na^+ solution ($Na^+_{out}/NMDG^+_{in}$, *Right*). Note the difference in current scale. (*B*) Superposition of normalized $NMDG^+$ (black trace) and Na^+ (gray trace) currents shown in *A* in logarithmic timescale. (*C*) Single-channel recordings from an outside-out patch recorded at –120 mV of currents elicited by 1 μM ATP, first in $NMDG^+_{out}/NMDG^+_{in}$ solution (*Left*), and then in $Na^+_{out}/NMDG^+_{in}$ solution (*Right*). Data were sampled at 10 kHz and filtered at a final corner frequency (f_c) of 1 kHz (*Top* traces) or 100 Hz (*Bottom* traces). Channel openings (o) are downward deflections indicated by the red dashed lines. Baseline currents, which correspond to closed channels (c), are indicated by the black dashed lines. (*D*) All-points amplitude histograms of single-channel Na^+ (*Top*, $f_c = 1$ kHz) and $NMDG^+$ currents (*Bottom*, $f_c = 100$ Hz) obtained from the patch shown in *C*. Distributions were fit by a sum of four Gaussians for Na^+ currents and three Gaussians for $NMDG^+$ currents (blue lines). Gaussians centered at 0 pA represent closed channels. For this patch, the mean unitary conductance of Na^+ currents in $Na^+_{out}/NMDG^+_{in}$ is 43 pS, whereas that of $NMDG^+$ currents in $NMDG^+_{out}/NMDG^+_{in}$ is 4.0 pS.

application. Increasing ATP concentration consistently decreased activation time constants (τ_{NMDG+} = 36 ± 4 ms, n = 10 patches at 10 μM; Fig. S1*B*). Consistent with a recent study (32), these data show that ATP rapidly gates an $NMDG^+$ conductance, which remains stable over time.

We next compared these $NMDG^+$ currents to those carried by Na^+ at the same potential, by rapidly exchanging (less than 1 s) external $NMDG^+$ for Na^+ (i.e., $Na^+_{out}/NMDG^+_{in}$), and then challenging again the same patch with 3 μM ATP. Robust inward Na^+ currents were recorded that were larger than $NMDG^+$ currents (I_{NMDG+}/I_{Na+} = 9.7 ± 1.7%, n = 9 patches; Fig. 1*A*, *Right*). This enhancement is expected, as the electrochemical driving force is in favor of Na^+ influx in $Na^+_{out}/NMDG^+_{in}$ solution. Comparison of normalized ATP-gated Na^+ currents to ATP-gated $NMDG^+$ currents revealed similar onsets of inward currents (Fig. 1*B*), quantified by similar activation rates (τ_{Na+} = 235 ± 74 ms at 3 μM ATP, n = 9; Fig. S1 *A* and *B*). Increasing ATP concentration also consistently decreased activation time constants (τ_{Na+} = 27 ± 4 ms at 10 μM, n = 10 patches; Fig. S1*B*), with no substantial change of the ratio I_{NMDG+}/I_{Na+} (11.4 ± 0.6%, n = 9). These results indicate that the ATP-gated P2X2 open pore is simultaneously permeable to both Na^+ and $NMDG^+$. The similarity of the activation rates determined in both solutions at a given ATP concentration suggests similar gating kinetics and that the difference in the current ratio must be due to different rates of permeation of these ions.

To determine $NMDG^+$ permeation rates, we measured unitary conductance of $NMDG^+$ current from outside-out patches that contained single channels, using the same protocols as described for patches that contained multiple channels. In $NMDG^+_{out}/NMDG^+_{in}$, barely visible single openings and closings were detected following 1 μM ATP application, whereas robust single-channel currents were recorded in $Na^+_{out}/NMDG^+_{in}$ (Fig. 1*C*, *Top*) with a mean conductance of 44 ± 8 pS (n = 7 patches, data filtered at 1 kHz). However, when the same recordings were further filtered at a much lower bandwidth (100 Hz; *Materials and Methods*), discernable unitary currents were then resolved in symmetric $NMDG^+$ solution (Fig. 1*C*, *Bottom*). These small unitary currents were always recorded in patches that responded to ATP in Na^+_{out} (16 out of 24 examined patches; the remaining 8 patches were unresponsive to ATP and no unitary $NMDG^+$ currents were detected), and they were not observed in the absence of ATP (Fig. S1*D*). All-points histogram analysis revealed that the mean conductance of these unitary currents was 3.3 ± 0.6 pS (mean amplitude of 0.40 ± 0.04 pA, n = 6 patches), which represented 7.5% of the unitary Na^+ currents, a value that was close to that of the ratio I_{NMDG+}/I_{Na+} determined from multichannel currents (Fig. 1*D* and Fig. S1*C*). Increasing ATP concentration to 10 or 30 μM did not change the ratio of the mean conductance of $NMDG^+$ relative to Na^+, suggesting that a near saturating concentration of ATP does not increase $NMDG^+$ conductance (Fig. S1*C*). Compared with recordings carried out in symmetric Na^+ solution (43 ± 6 pS, n = 4 patches at 1 μM ATP; Fig. S1*E*), the unitary conductance of $NMDG^+$ currents was about 13 times lower than that of Na^+ currents. From these values, we conclude that $NMDG^+$ ions flow through the ATP-gated open pore at extremely low rates (~2.5×10^6 $NMDG^+$ ions per second per channel at –120 mV with 132.6 mM $NMDG^+$) compared with Na^+ (~32×10^6 Na^+ ions per second per channel at –120 mV with 132.6 mM Na^+). Given the fact that $NMDG^+$ can rapidly transit through the ATP-gated receptor channel, our data demonstrate that the open pore is wide enough to allow its passage on the millisecond time scale.

Molecular Motions Underlying $NMDG^+$ Permeation Are Similar to Those Underlying Na^+ Permeation. We next sought to determine the molecular motions that drive permeation of $NMDG^+$. We used our recent "opto-tweezers" strategy, which enabled us to probe the gating mechanism of P2X2 receptors by using light to open and close the pore (36). This strategy entails the use of a synthetic semirigid azobenzene cross-linker, 4,4′-bis(maleimidoglycine) azobenzene, called MAM (named hereafter MAM-3), which is covalently tethered between a pair of engineered cysteine-substituted residues located at an appropriate distance apart. Light stimulation at specific wavelengths can then be used to force parts of the protein to come closer together or move farther apart due to isomerization of the azobenzene between defined *trans* and *cis* configurations (Fig. 2 *A* and *B*). These light-driven motions provide a faithful readout of the molecular movements induced by ATP (36, 37).

We focused on the region of the pore that is particularly effective for manipulating molecular motions by light—that is, around residues I328 and S345, which can be cross-linked horizontally or vertically relative to the membrane plane by MAM-3 (36) (Fig. 2*C*). To increase the chance of trapping any incremental change of the pore diameter, we synthesized two shorter, more rigid photo-switchable cross-linkers, named MAM-1 (also known as BMA) (37) and MAM-2, in which the cysteine-reactive maleimides are either directly attached to both extremities of the azobenzene core (MAM-1) or indirectly at one of the two extremities by a glycine unit (MAM-2) (Fig. 2*A* and Figs. S2–S4). As a result, the two end-to-end maleimides are incrementally separated by 2 Å between any two consecutive MAMs in their *trans* configuration (Fig. S5). The end-to-end distance distributions in the *cis* configuration were significantly broader and more difficult to interpret. We produced 13 single and double cysteine mutants in the P2X2–3T background that were expressed in HEK-293 cells and individually treated with each photo-switchable cross-linker, giving rise to 42 different combinations, including controls on the P2X2–3T (Fig. 2*E*). Effects of light on receptor activity were then assayed using whole-cell patch-clamp recordings on 365-nm (80 ms or 2 s, 17.7 mW/mm^2), 530-nm (2 or 4 s, 13.3 mW/mm^2), or 455-nm (2 s, 39.5 mW/mm^2) illumination cycles to elicit photocurrents in symmetric $NMDG^+$ solutions. These currents were normalized to those carried by Na^+ (I_{NMDG+}/I_{Na+}), following the rapid exchange of cells to an $Na^+_{out}/NMDG^+_{in}$ solution.

The screening revealed four important findings. First, all mutants responded to ATP and were permeable to $NMDG^+$ when ATP was used as an agonist, with I_{NMDG+}/I_{Na+} ratios that were similar to those recorded in outside-out patches (between 4% and 15%; Fig. 2*E*, Fig. S6*A*, and Table S1). In control experiments, no light-gated currents were observed with P2X2–3T incubated with any MAM (Fig. 2*E* and Fig. S6*B*). Second, only a few of the cysteine mutants (7 combinations out of 39) showed reliable light-induced $NMDG^+$ currents, with a I_{NMDG+}/I_{Na+} ratio > 5 (mean 9 ± 3%) that was close to that of ATP controls (Fig. 2*E*). Indeed, most of the cysteine mutants responded to light following incubation with MAMs (27/39), but control experiments revealed that many of the light-gated currents originating from double mutants (12/19) had activation profiles that were similar to those of one of their single-mutant counterparts (asterisk-labeled boxes in Fig. 2*E*). In addition, two other combinations—I332C/F346C incubated with MAM-2 or MAM-3—which displayed the highest I_{NMDG+}/I_{Na+} ratios, were discarded because MAM treatment appeared to dramatically reduce light-gated Na^+ currents, which, in turn, may introduce uncertainty regarding ratio measurements (Fig. 2 *D* and *E*).

Third, two phenotypes were observed in light-induced $NMDG^+$ currents: Horizontally cross-linked single mutants (I328C treated with MAM-2 or MAM-3, and I332C treated with MAM-1) were activated in the *trans* configuration of the azobenzene, leading to an $NMDG^+$ permeability, whereas vertically cross-linked double mutants (I328C/S345C treated with any MAMs, and I332C/S345C treated with MAM-2) were activated in the *cis* configuration (Fig. 2 *D* and *E*). Conversely, backward isomerization of the

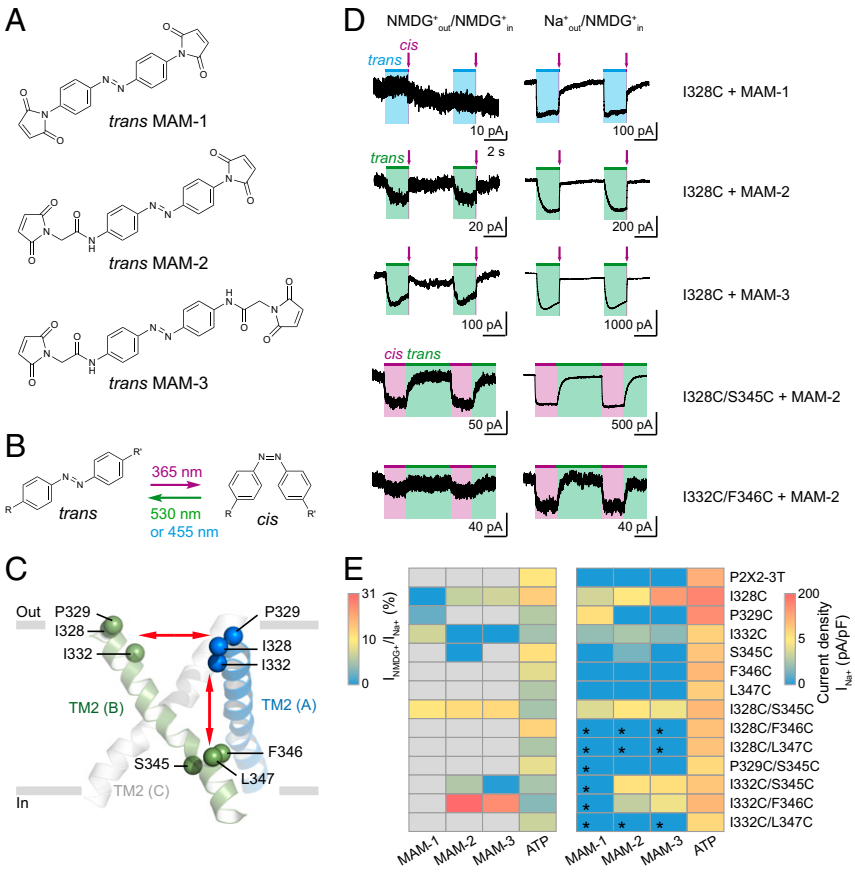

Fig. 2. $NMDG^+$ permeation operates with similar molecular motions to Na^+ permeation. (*A*) Chemical structures of MAMs in the *trans* state. (*B*) *Cis–trans* isomerization of the azobenzene induced by the indicated wavelengths of light. The backward *cis–trans* isomerization is induced by irradiation at 455 nm for MAM-1 or 530 nm for MAM-2 and MAM-3. (*C*) Side view of the three transmembrane TM2 helices of the hP2X3 ATP-bound X-ray structure [Protein Data Bank (PDB) ID code 5SVK] (10) shown in ribbons and color-coded by subunit. Residues selected for cysteine substitution are indicated by spheres on monomers A and B, and for clarity, they were converted to equivalent rP2X2 numbering. Double red arrows indicate possible horizontal and vertical MAMs cross-linking, relative to the membrane plane, between engineered cysteines. (*D*) Macroscopic light-gated currents recorded at –60 mV from HEK-293 cells expressing the indicated mutants treated with the indicated MAMs. Cells were first bathed in extracellular $NMDG^+$ solution ($NMDG^+_{out}/NMDG^+_{in}$, *Left*), which was then rapidly exchanged for extracellular Na^+ solution ($Na^+_{out}/NMDG^+_{in}$, *Right*). Illumination was carried out, as indicated, at 365 nm (violet bars) and 455 nm (blue bars) or 530 nm (green bars) to elicit the *cis* and *trans* states of the azobenzene, respectively. Short illuminations (80 ms) are indicated by violet arrows. For MAM-treated single mutants, cells were briefly preirradiated at 365 nm (80 ms) before recordings. (*E*) Heat map of $NMDG^+$ currents normalized to Na^+ currents (*Left*) and of Na^+ currents density (*Right*) recorded in indicated conditions. All light-gated currents recorded for single mutants were induced by the *trans* configuration, whereas all light-gated currents recorded for double mutants were elicited by the *cis* configuration, except those indicated by asterisks, which responded to the *trans* configuration, similarly to their single mutant counterparts I328C, P329C, or I332C. Gray boxes indicate that I_{NMDG+}/I_{Na+} cannot be determined. In controls, 30 μM ATP, applied on untreated cells, elicited responses that range between 32% and 92% of the maximal response (see Table S2) (for each box, n = 4–7 cells).

azobenzene from *trans* to *cis*, in the case of horizontally cross-linked mutants, or *cis* to *trans* configuration, for vertically cross-linked mutants, closed the pore, and an additional illumination cycle revealed full reversibility of the light-gated $NMDG^+$ currents. Supported by intersubunit cross-linking (Fig. S6*C*), these data demonstrate that the opening of the $NMDG^+$-permeable pore involves two molecular motions: (*i*) a specific vertical shortening of the distance between extracellular and intracellular ends of adjacent TM2 helices, and (*ii*) an outward separation of the extracellular ends from two adjacent TM2 helices.

Fourth, a clear correlation between light-gated $NMDG^+$ and Na^+ currents was observed, whereby Na^+ currents were always observed in the case of $NMDG^+$ currents, and inversely, no light-gated $NMDG^+$ currents were recorded when no light-gated Na^+ currents were recorded, indicating that the molecular mechanism underlying $NMDG^+$ permeation is very similar to that underlying Na^+ permeation.

Unlike our previous work (36), we found substantial $NMDG^+$ permeability in mutant I328C cross-linked horizontally with MAM-3. The reason for this discrepancy is unknown, but given that $NMDG^+$ permeability had been obtained by measuring E_{rev} from bi-ionic experiments (36), it remains possible that its permeability was underestimated, further stressing the need to use symmetric solutions to measure direct permeation events.

Occurrence of Partially Open States. The correlation between light-gated $NMDG^+$ and Na^+ currents was, however, not perfect. The results revealed that in 3 out of 11 combinations that displayed sizeable light-gated Na^+ currents (current density > 3 pA/pF), no or very small light-gated $NMDG^+$ currents were recorded (I_{NMDG+}/I_{Na+} were equal or close to zero; Fig. 2*E*). These data were observed in both vertical (I332C/S345C treated with MAM-3) and horizontal (I328C and P329C treated with MAM-1) cross-linking. Of note, increasing the length of the "tweezers" in the horizontal I328C cross-linking from MAM-1 to MAM-2 to MAM-3 increased the ratio I_{NMDG+}/I_{Na+} from 0% to ~7% (Fig. 2*D*). Likewise, decreasing the length of the tweezers in the vertical I332C/S345C cross-linking from MAM-3 to MAM-2 also increased the ratio

I_{NMDG+}/I_{Na+} from ~0.2% to ~6%. Although we cannot rule out the hypothesis that the presence of MAM is specifically interfering with the bulkier $NMDG^+$, these data suggest the existence of partially, Na^+-selective open states that are not permeable to $NMDG^+$.

Light-Induced Motions Gate Dye Uptake in Physiological Conditions. To further confirm data obtained by patch-clamp electrophysiology, we measured YO-PRO-1 dye uptake in physiological conditions, where Na^+ replaced $NMDG^+$. We focused on the pair I328C and S345C treated with MAM-2, which gave both the highest I_{NMDG+}/I_{Na+} ratio and the most robust light-gated Na^+ current density. Robust dye uptake following a pulse of 5 s of light at 365 nm was observed for the double mutant I328C/S345C (Fig. 3 *A* and *C*). These uptakes were light-dependent and were similar to those induced by 30 μM ATP on the P2X2–3T background (Fig. 3 *A* and *B*). In contrast, no dye uptake was observed in cells expressing the single mutant I328C or S345C incubated with MAM-2 that were illuminated at 530 nm, following a brief preirradiation at 365 nm before YO-PRO-1 application to reset the azobenzene in the *cis* state (Fig. 3 *D* and *E*). Although these fluorescence data were in agreement with patch-clamp data, the lack of YO-PRO-1 intake for I328C seemed to be in contrast to the recorded $NMDG^+$ permeability. However, a careful analysis showed a rapid inactivation of light-gated currents during and after irradiation of cells expressing the I328C mutant treated with MAM-2, whereas stable light-gated currents were recorded for the double mutant I328C/S345C incubated with the same photo–cross-linker (Fig. S7). The transient light-gated activation of the single mutant likely prevents substantial accumulation of YO-PRO-1 into cells, a hypothesis that readily explains the apparent lack of dye uptake. All together, these results provide evidence that YO-PRO-1 uptake induced by the *cis* configuration of MAM-2 tethered to the I328C/S345C double mutant occurs in physiological conditions.

MD Simulations of $NMDG^+$ Permeation. To obtain insights into the permeation mechanism of large organic cations in P2X receptors, $NMDG^+$ conductance was explored by all-atom MD. For this purpose, an atomistic model of the open state of zfP2X4 equilibrated with three MAM-2 vertically cross-linked between I336C and N353C (i.e., equivalent to I328C and S345C in rP2X2) was simulated in the presence of a membrane potential generated by a constant electric field (*Materials and Methods*). To capture $NMDG^+$ permeation events on the simulation time scale (i.e., <50 ns), the ion channel devoid of the extracellular domain was simulated in the presence of a large membrane potential (up to –2 V) in the absence of MAM and with harmonic restraints on the backbone atoms to preserve its open-pore conformation. The MD results show that our open-state model of zfP2X4 is permeable to $NMDG^+$ (Fig. 4 and Movie S1) with a permeation rate of 7×10^7 s^{-1}, which is approximately one order of magnitude lower than that simulated in the presence of Na^+ (Table S1). Of note, these results closely match the ratio measured from single-channel recordings, although the absolute values obtained from modeling were largely higher than those determined experimentally. This is likely due to the nonphysiological value of the electrochemical driving force that was used in MD. These simulations reveal that the difference in permeability observed for Na^+ versus $NMDG^+$ is due to a more complex permeation mechanism for the latter, which involves a selection for permeation based on both the molecular conformation and the orientation of the organic cation relative to the pore axis. In fact, by monitoring the end-to-end distance and the orientation of $NMDG^+$ along a series of successful permeation events sampled by MD, we found that to be able to cross the constriction point, the organic cation must adopt a fully extended conformation (d > 7.5 Å) and have the charged nitrogen atom facing downward along the electrochemical gradient ($\theta < -50°$) (Fig. 4). In addition, the simulations indicated that before populating a permeable conformation, the flexible $NMDG^+$ needs to sample several conformations and orientations, which significantly hinders its permeability, consistent with low unitary conductance of single-channel $NMDG^+$ currents. Hence, the simulation results confirm that the open-channel state elicited by MAM is permeable to $NMDG^+$ and provide an atomistic picture of the permeation mechanism.

Permeation of YO-PRO-1 was also investigated by MD; however, in sharp contrast to results obtained for $NMDG^+$, no permeation event was sampled under similar simulation conditions (see Table S1).

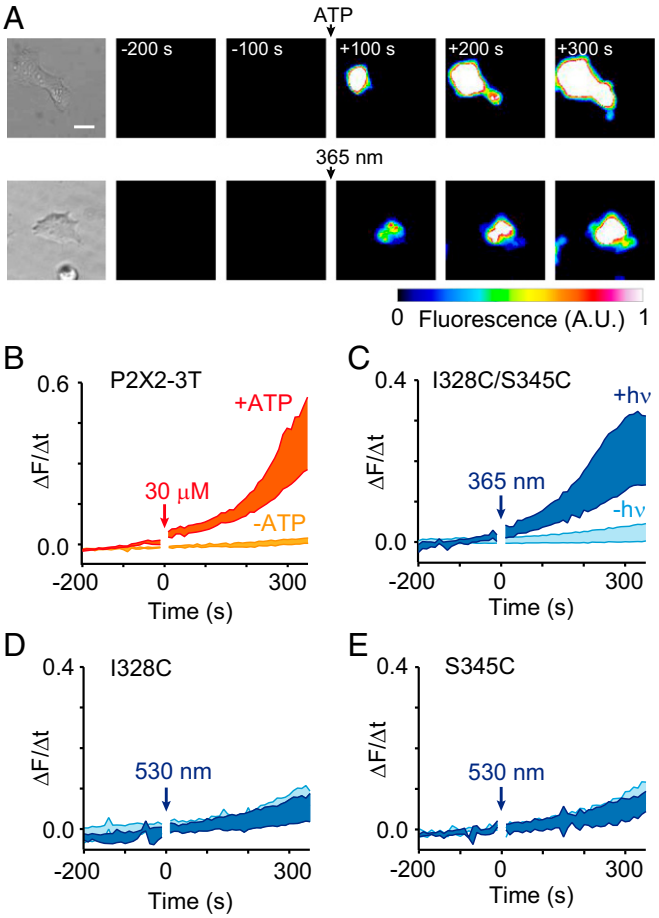

Fig. 3. Structural changes of TM2 helices induce cellular dye uptake in physiological conditions. (*A*) Selected time series of YO-PRO-1 dye uptake in HEK-293 cells expressing the P2X2–3T receptor (*Upper*) and double mutant I328C/S345C treated with MAM-2 (*Lower*). Fluorescence (in arbitrary units) was acquired before and during ATP (30 μM) or light (365 nm for 5 s) activation that started at 0 s as indicated. On the left are shown the corresponding microphotographs under transmitted light. (Scale bar, 20 μm.) (*B*) Corresponding rate of YO-PRO-1 dye uptake in cells ($n = 15$ cells) expressing the P2X2–3T receptor in the absence (orange) or presence (red) of ATP. The arrow indicates the time at which ATP was applied. (*C*) Corresponding rate of dye uptake in cells expressing the double mutant I328C/S345C treated with MAM-2 in the absence (light blue) or presence (dark blue) of irradiation at 365 nm ($n = 18$ cells). The arrow indicates the time at which cells were briefly irradiated. (*D*) Same protocol as in *C* for cells expressing the single mutant I328C treated with MAM-2, except that irradiation occurred at 530 nm ($n = 12$ cells). (*E*) Same protocol as in *D* for cells expressing the single mutant S345C treated with MAM-2 ($n = 18$–21 cells). For *D* and *E*, cells were briefly preirradiated at 365 nm for 2 s just before YO-PRO-1 application. Shaded areas denote mean ± SEM.

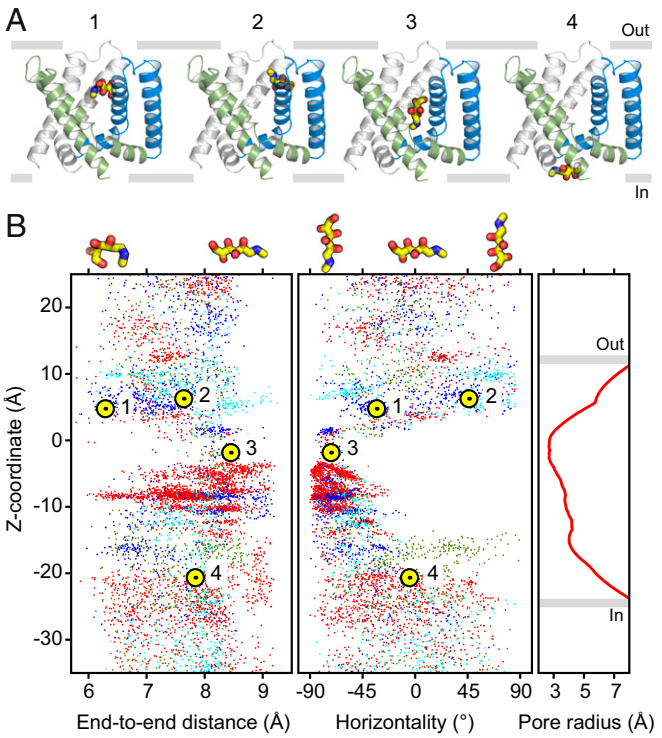

Fig. 4. Mechanism of $NMDG^+$ permeation revealed by MD simulations. (*A*) Snapshots at different simulation times. (*B*) End-to-end distance of $NMDG^+$ (*Left*) and angle formed by the longitudinal axis of $NMDG^+$ cation with the axis parallel to the membrane plane (*Middle*) are displayed per frame of the simulation for all permeant molecules. Data were collected from four different $NMDG^+$ concentration and membrane potential simulation setups: 1 M at –1 V (red dots), 0.15 M at –1 V (green), 0.15 M at –1.5 V (blue), and 0.15 M at –2 V (cyan). Molecular snapshots of $NMDG^+$ conformations and orientations corresponding to extreme values for these two observables are shown on top. Indicated numbered dots in yellow are snapshots from *A*. HOLE profile of the zfP2X4 open-state model after 50 ns of equilibration (*Right*). The simulation results indicate that the ion pore of the ATP-bound state is sufficiently wide to allow for the passage of large organic cations.

Selected Homomeric P2X Receptors Conduct Large Natural Molecules in Response to ATP. Our data reveal that the permeability to large cations develops within milliseconds upon ATP application, with the same time course as permeability to small cations. We thus asked whether this process is also true for other P2X members, especially for the fast-desensitizing P2X1 and P2X3 receptors, which were presumed to be "nondilating." To this end, we recorded ATP-gated currents in HEK cells transfected with rat P2X1, P2X3, P2X4, P2X5, P2X7, and human P2X2 and P2X3 receptors in symmetric $NMDG^+$ solutions (Fig. 5*A* and Fig. S8). We observed fast and robust $NMDG^+$ currents for all these P2X receptors, expect for P2X1, which for unknown reasons was not functional in symmetric $NMDG^+$ solution (no ATP-gated current was observed in the control solution $Na^+_{out}/NMDG^+_{in}$). Importantly, we provide evidence that $NMDG^+$ can permeate the rat and human P2X3 receptors, demonstrating that these desensitizing P2X receptors do indeed carry the ability to rapidly enter a state that is wide enough to allow the passage of large molecules.

Finally, having shown that rapid activation of P2X receptors allows permeation of $NMDG^+$, we sought to determine which natural compounds can transit through the pore. We focused on positively charged compounds that share a similar size to $NMDG^+$. We selected spermidine, which is a natural polyamine known to modulate many ion channels (38), and produced symmetric spermidine solutions (*Materials and Methods*). We observed robust inward spermidine whole-cell currents following rapid application of ATP in cells expressing the human P2X2 and P2X3 receptors while the membrane was held at –60 mV (Fig. 5*B*). Of note, MD simulations show that the ATP-bound, zfP2X4 open state is also permeable to spermidine (Movie S2). In addition, the simulations indicate that its permeation rate (5×10^8 s^{-1}) is sevenfold faster than that of $NMDG^+$ under the same membrane potential. The symmetrical structure of spermidine in addition to the presence of positive charges at the extremities make both the conformational and orientational barriers for permeation almost vanish, thus drastically enhancing its permeability relative to $NMDG^+$ despite their similar size. These data therefore uncover a previously unappreciated P2X signaling in which large molecules can rapidly permeate through the pore in response to ATP binding.

Discussion

In this article we uncover the molecular mechanism underlying the permeability of P2X receptors to large organic cations and identify an important natural ion channel modulator able to flow through the ATP-gated pore. Our data tackle the pore dilation paradigm, which has remained for nearly 20 years one of the most enigmatic features of ionotropic purinergic receptors (19, 20). Until recently, the dogma concerning pore dilation was that the channel undergoes a progressive expansion, over time reaching a diameter wide enough to allow permeation of large cations, such as $NMDG^+$ and YO-PRO-1. However, a recent study challenged this model by elegantly demonstrating that P2X channels rapidly develop an

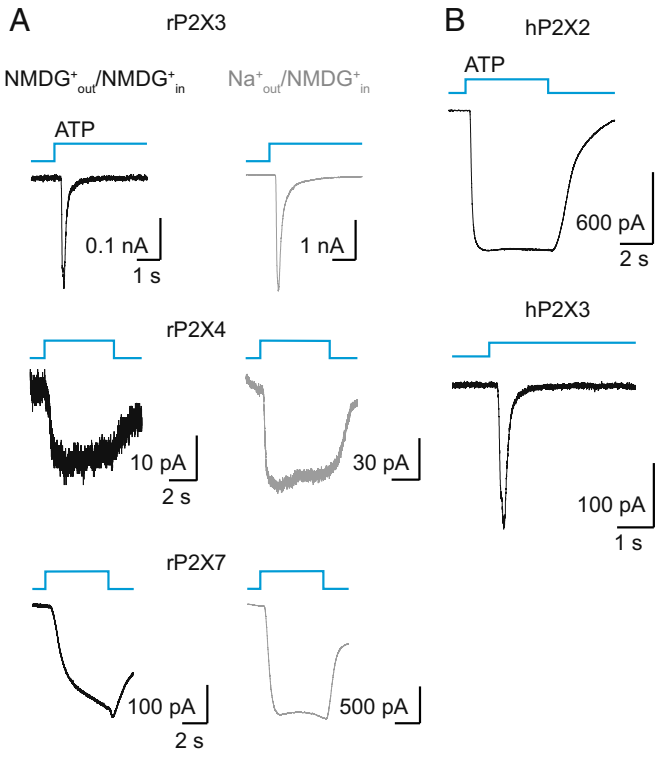

Fig. 5. P2X receptors are permeable to natural organic cations. (*A*) Macroscopic ATP-gated currents recorded at –60 mV from HEK-293 cells expressing the indicated rat P2X receptors. Recordings were first made in symmetric $NMDG^+_{out}/NMDG^+_{in}$ solution (black traces) and then in $Na^+_{out}/NMDG^+_{in}$ (gray traces) solution. ATP concentration was 30 μM for rP2X3 and rP2X4 and 300 μM for rP2X7 receptors. For rP2X3 receptors, ATP applications were spaced at least by 3 min. (*B*) Macroscopic ATP-gated currents recorded in symmetric spermidine solution at –60 mV from HEK-293 cells expressing the indicated human P2X receptors. ATP concentration was 30 μM. Spermidine current density was as follows: hP2X2, 43 ± 4 pA/pF (n = 5 cells); hP2X3, 6 ± 2 pA/pF (n = 7 cells). For all traces, ATP application lasted 5 s.

$NMDG^+$ current upon ATP binding and lack the slow phase of pore dilation (32). Our results are consistent with this work, and taken together, these two studies firmly establish that, in striking contrast to earlier beliefs, the open state that is reached in milliseconds following ATP binding is also permeable to large molecules. This important finding raises considerable questions concerning the previously predominant view that suggested that the initial I_1 open state is only selective to small cations, such as Na^+, K^+, and Ca^{2+}. The immediate implication of our results is that the structure of the open pore of the ATP-bound state must be sufficiently wide to accommodate large molecules. From the X-ray structures of the ATP-bound zfP2X4 receptor (8) and very recently the ATP-bound human P2X3 (hP2X3) receptor (10), this seems to be the case, as the minimal cross-section of an extended $NMDG^+$ (6 Å × 6 Å × 12.5 Å) is less than the diameter of the open pore (~7 Å for zfP2X4 and 6.4 Å for hP2X3). However, reliable $NMDG^+$ permeation by MD simulations cannot be made on the zfP2X4 X-ray structure because the pore systematically collapses within a few nanoseconds (<5) of equilibration (36), likely due to the lack of the intracellular domain that was removed for crystallization purposes (8). By using an improved model of the open state of zfP2X4 (36), which was equilibrated by 50-ns MD in a physiological environment and stabilized by three vertically cross-linked MAM-2 molecules, we provide clear evidence that both $NMDG^+$ and the natural cation spermidine may flow through the ion pore of the ATP-bound state. We found, however, that the flow of $NMDG^+$ was significantly lower than that of Na^+, as the former needs to "snake" through the permeating pathway in a fully linear conformation, with the positively charged nitrogen head group pointing downward along the electrochemical gradient. The conformational confinement to this extended form, along with specific orientational constraints in the narrowest region of the pore, introduces significant barriers that hinder cation permeability, thus revealing a complex mechanism for $NMDG^+$ permeation. These molecular requirements therefore cause a decrease in the overall rate of $NMDG^+$ flow. This conclusion is fully consistent with the low unitary conductance of single-channel $NMDG^+$ currents that we (present study) and others (16, 33, 39) have measured for P2X2 and P2X7 receptors.

In contrast to $NMDG^+$, we were unable to sample permeation events for YO-PRO-1 in MD simulations. Because the minimal cross-section of the dye (7 Å × 8 Å × 19 Å) reaches the outer limits of the open pore (~7 Å), it is possible that YO-PRO-1 needs to sample more conformations and orientations before a successful permeation can occur, a process that would take considerably more time. As a result, the flux of this fluorescent dye would be extremely low, likely below that of $NMDG^+$. Such a molecular sampling-limited step may help to explain the apparent delayed entry of fluorescent dyes that were typically used for monitoring dye uptake through P2X receptors.

An important finding of this study is that the molecular motions driving $NMDG^+$ conductance are very similar to those that lead to Na^+ flow. By using our recently reported opto-tweezers approach (36), we tested the ability of three photo-switchable cross-linkers of different lengths to optically control $NMDG^+$ permeability of 13 cysteine mutants. We observed reliable $NMDG^+$ permeation with only 7 out of the 39 tested combinations and found a clear correlation between light-gated $NMDG^+$ currents and light-gated Na^+ currents. The specificity of cross-linked residues and the size dependence of the MAMs strengthen the conclusion that the used tweezers do not induce disorder in the protein but rather can be used as mechanical actuators to justly monitor naturally relevant motions. We identified two molecular motions that lead to permeation of large organic cations: a horizontal outward separation of the extracellular ends of TM2 helices and a vertical motion, in which the *N* and C termini of TM2 helices from adjacent subunits come closer together or change their orientations relative to one another, most likely through a change of the helical structure. Importantly, such similar molecular motions were also identified during channel gating (36), suggesting that ATP binding drives the rapid opening of a pore that is simultaneously selective to both small and large cations. As we do not have evidence for a time-dependent increase of the permeability of large cations, our data thus support the conclusion that pore dilation is not an intrinsic property of the channel itself. However, we do not rule out the possibility that pore dilation does exist, but if this were the case, it must require a regulatory element that is external to the P2X pore and that would be lost in our experimental conditions.

One intriguing feature of the mechanism revealed by the opto-tweezers approach is that it raises the possibility to open the channel in a state that is not fully open. We found that an insufficient horizontal outward separation or inappropriate vertical motions of two adjacent TM2 helices failed to open $NMDG^+$ conductance but not Na^+ conductance, suggesting that the pore is partially open. A further variation, by only a few Å, of adjacent helices induced an $NMDG^+$ permeation in addition to the Na^+ flow, thus allowing the pore to become fully opened. The physiological relevance of these partially open states remains unclear, but they might be related to dynamic changes of other biophysical properties of P2X receptors, such as ATP potency and rectification, as reported previously (40, 41). Another possibility would be that these partially open states might correspond to the actual I_1 state. However, we do not favor this hypothesis because we provide no evidence that ATP binding naturally drives the opening of the channel in partially open states that are only selective to small cations.

Finally, we have identified spermidine as a natural cation able to permeate through the ATP-gated open state. Polyamines are well-known to modulate the activity of many ion channels, including synaptic ligand-gated ion channels (38). Importantly, we show that even desensitizing receptors, such as hP2X3, which have been considered thus far as nondilating pores, are able to briefly activate their pores in an open state, allowing for a transient flow of spermidine. This finding has considerable physiological significance because it discloses an unsuspected role of polyamines in P2X signaling and more generally because it raises the possibility that activation of P2X receptors may allow for the exchange of other physiological molecules between cells, such as amino acids. Notably, a recent study exploited the large-pore property of P2X receptors to deliver small membrane-impermeable drugs to diseased retina cells (42). We thus propose that besides the critical role of the permeation of inorganic cations, the passage of small-sized metabolites, like spermidine, through the ATP-gated open P2X pore may contribute to alternative physiological responses. These findings open up new horizons in P2X signaling.

Materials and Methods

Chemical Synthesis. All chemicals were purchased from Sigma-Aldrich, Fluka, Across, or Alfa Aesar in analytical grade. An Agilent LC–MS RRLC 1200SL/ESI QTof 6520 was used for ESI analysis. ^1H NMR and ^{13}C NMR were run at 400 and 100 MHz, respectively, on an Avance^{III} 400 NMR spectrometer from Brucker. Coupling constants (*J*) are quoted in Hz and chemical shifts (δ) are given in parts per million (ppm) using the residue solvent peaks as reference relative to tetramethylsilane (TMS).

For MAM-1 synthesis, 498 mg (2.348 mmol) of (*E*)-4,4′-(diazene-1,2-diyl) dianiline and 462.3 mg (4.715 mmol, 2 eq) of maleic anhydride were mixed in 20 mL of anhydrous THF and left 1 h at 4 °C. The resulting product was centrifuged (4 min, 8,000 *g*), and the precipitate was resolubilized in 20 mL of anhydrous THF. Then, 0.5 mL (5.324 mmol, 2.3 eq) of acetic anhydride and 50.2 mg of sodium acetate were added. The mixture was heated under microwave conditions (20 min, 110 °C). Distilled water was added (100 mL), and after centrifugation (10 min, 8,000 *g*), the precipitate was resolubilized in 100 mL of methanol and an orange solid was obtained by slowly adding cold water. After filtration, purification was carried out by Flash-column chromatography (silica) with dichloromethane and ethyl acetate (gradient 100:0 ≥ 95:5). After evaporation of the solvent, the pure MAM-1 was obtained as a bright orange solid (36% yield): NMR ^1H ($CDCl_3$):δ (ppm), 8.01 (4H, d, $J = 8.8$ Hz), 7.55 (4H, d, $J = 8.8$ Hz), and

6.88 (4H, s); NMR ^{13}C ($CDCl_3$):δ (ppm), 169.16, 151.23, 134.42, 133.72, 126.22, and 123.70; and (ESI-HMRS):(*m/z*, $[M+H]^+$), calculated for $C_{20}H_{13}N_4O_4^+$, 373.0859; found, 373.0932.

For synthesis of intermediate 1, 398 mg (1.875 mmol) of (*E*)-4,4′-(diazene-1,2-diyl)dianiline and 726.8 mg (4.7 mmol, 2.5 eq) of 2-(2,5-dioxo-2, 5-dihydro-1H-pyrrol-1-yl)acetic acid were solubilized in a mixture of anhydrous DMF/acetonitrile. We then added 1.108 g (4.7 mmol, 2.5 eq) of HATU and 0.65 mL of anhydrous triethylamine (4.7 mmol, 2.5 eq). The mixture was agitated at room temperature for 20 h. After extraction ($NaHCO_3$, 3× ethyl acetate), the crude product was washed with acetone. The supernatant was purified by flash-column chromatography (silica) with ethyl acetate and heptane (60:40). An orange product was obtained (compound 1, 51% yield): NMR ^1H (acetone-d_6):δ (ppm), 9.66 (1H, s), 7.78 (2H, d, J = 9.3 Hz), 7.76 (2H, d, J = 9.3 Hz), 7.71 (2H, d, J = 8.9 Hz), 7.01 (2H, s), 6.78 (2H, d, J = 8.9 Hz), and 4.41 (2H, s); NMR ^{13}C (DMSO-d6):δ (ppm), 170.64, 165.11, 152.47, 139.70, 138.55, 136.20, 134.95, 128.15, 125.90, 123.50, 122.23, 118.86, 112.85, 112.52, 68.49, 55.81, 32.08, and 29.58.

For synthesis of MAM-2, 200 mg (0.5725 mmol) of intermediate **1** was mixed with 112.3 mg (1.145 mmol, 2 eq) of maleic anhydride and heated under microwave conditions (110 °C, 90 min) in acetone. The obtained precipitate was filtered and resuspended in acetone and then heated 5 min at 60 °C with 0.12 mL of triethylamine (0.8588 mmol, 1.5 eq). We then added 0.54 mL of acetic anhydride (5.725 mmol, 10 eq) with a catalytic amount of manganese acetate (III), and the mixture was heated under microwave conditions (90 min, 110 °C). After addition of water and filtration, 46.1 mg of MAM-2 was obtained (19% yield): NMR ^1H (DMSO-d6):δ (ppm), 10.66 (1H, s), 7.97 (2H, d, J = 8.8 Hz), 7.92 (2H, d, J = 8.8 Hz), 7.79 (2H, d, J = 8.8 Hz), 7.58 (2H, d, J = 8.8 Hz), 7.23 (2H, s), 7.16 (2H, s), and 4.34 (2H, s); NMR ^{13}C (acetone-d6):δ (ppm), 171.30, 170.38, 166.17, 152.11, 149.51, 142.76, 135.71, 135.60, 135.25, 127.78, 124.83, 123.80, 120.53, and 41.46; (ESI-HMRS):(*m/z*, $[M+H]^+$), 429.1073 calculated for $C_{22}H_{15}N_5O_5^+$; found, 429.1069.

The synthesis of MAM-3 was carried out as previously described (36).

Molecular Biology. Cysteine mutations were introduced into a rP2X2 receptor background in which Cys9, Cys348, and Cys430 were mutated to threonine (P2X2–3T) (35) using KAPA HiFi HotStart PCR kit (Cliniscience). All mutations were confirmed by DNA sequencing (GATC-Biotech). All P2X encoding genes were subcloned in pcDNA3.1 vector, except that encoding hP2X2, which was subcloned in the vector pCMV6-AC-mGFP (OriGene). hP2X2 contains mGFP at its C terminus.

Expression in Cultured Cells. HEK-293 and TSA-201 cells were cultured and transiently transfected using phosphate calcium procedure with the pcDNA3.1(+) vectors (0.05–0.1 μg for single channel recordings, 0.3 μg for whole-cell recordings, and 10 μg for cell surface cross-linking) and a vector encoding a green fluorescent protein (0.3 μg), as previously described (43).

Patch-Clamp Electrophysiology. Single-channel recordings using outside-out configuration were carried out using HEK-293 cells at room temperature 24 h after transfection. Recording pipettes pulled from borosilicate glass (Harvard Apparatus) were coated with Sylgard 184 (Dow Corning Co.) and fire polished to yield resistances of 10–20 MΩ (Sutter model p-97). The holding potential was –120 mV. The extracellular solution contained 132.6 mM NaCl or NMDG (Sigma), 0.3 mM $CaCl_2$, 0.25 mM $MgCl_2$, 10 mM Hepes, pH 7.3, adjusted with NaOH (for NaCl solution) or HCl solution (for NMDG solution). The intracellular solution contained either 132.6 mM NMDG, 9.46 mM Hepes, and 10 mM EDTA, adjusted to pH 7.3, first approximately with a 5% HF solution, then more precisely with 0.5% HF with Polypropylene (PP) pipettes (Dominique Dutscher) or 132.6 mM NaF, 9.46 mM Hepes, and 10 mM EDTA, adjusted to pH 7.3 with NaOH. Osmolarity was adjusted to 290–310 mOsmol·kg^{-1} with glucose. Data were acquired with a patch-clamp amplifier (HEKA EPC 10) using PATCHMASTER software (HEKA Co.), sampled at 4–10 kHz, and low-pass filtered at 2.9 kHz. For offline analysis, data were refiltered to give a cascaded filter corner frequency (f_c) of either 1 kHz or 100 Hz. For data analyses, FitMaster (HEKA Electroniks, v2 × 73.2) and IGOR PRO (WaveMetrics, v6.37A) softwares were used. Channel events were detected by using TAC software (Bruxton Co.), and conductance levels were measured by all-points amplitude histograms fitted to Gaussian distributions. Fitting procedures to access the time constant were based on the single-exponential decay equation function, $I_t = I_0 + A \exp(-t/\tau)$, where I_t is the instantaneous current; I_0 and A are the residual current and maximal amplitude, respectively; t is the time in seconds; and τ is the time constant in seconds.

Whole-cell recordings were performed 24–48 h after transfection in HEK-293 cells. Normal external solution (NES) contained 140 mM NaCl, 2.8 mM KCl, 2 mM $CaCl_2$, 2 mM $MgCl_2$, 10 mM glucose, 10 mM Hepes, adjusted to pH 7.3 with NaOH. Normal internal solution (NIS) contained 140 mM KCl, 5 mM $MgCl_2$, 5 mM EGTA, 10 mM Hepes, adjusted to pH 7.3 with NaOH. For MAMs incubation, cells were incubated before recordings at room temperature with, respectively, MAM-1 (10 μM for 5 min, 1% final concentration of DMSO in NES), MAM-2 (10 μM for 10 min, 1% DMSO in NES), and MAM-3 (3 μM for 20 min, 1% DMSO in NES) and 3 μM ATP. After treatment, cells were washed out with NES. Patch pipettes contained 140 mM NMDG, 10 mM Hepes, and 10 mM EDTA, pH adjusted with HCl to 7.3. To measure $NMDG^+$ permeation, extracellular solution contained 140 mM NMDG and 10 mM Hepes, pH 7.3. The solution was then exchanged to NaCl solution containing 140 mM NaCl and 10 mM Hepes, pH 7.3. For control experiments, these solutions were supplemented with 30 μM ATP. For spermidine permeation experiments, whole-cell recordings were performed 24–48 h after transfection. Patch pipettes contained 33 mM spermidine, 10 mM Hepes, and 10 mM EDTA, pH adjusted to 7.3 with HCl. The extracellular solution contained 33 mM spermidine and 10 mM Hepes, pH 7.3, supplemented with 30 μM ATP. Osmolarity of all these solutions was adjusted as described above. Current density was obtained by dividing the current by the cell membrane capacitance.

Cell-Surface Cross-Linking. Cross-linking of cell-surface receptors was performed as follows. TSA-201 cells in dishes were transfected with pcDNA3.1(+) vectors containing the mutant constructs. After 24 h or 48 h, cells in dishes were washed with ice-cold PBS that contained 154 mM NaCl, 2.68 mM KCl, 4.2 mM Na_2HPO_4, 1.47 mM KH_2PO_4, pH 7.0, supplemented with 1 mM $MgCl_2$ and 0.4 mM $CaCl_2$. Then, cells were incubated under gentle agitation with 50 μM photo-switchable cross-linker in the presence of 3 μM ATP in ice-cold PBS, for 20 min (MAM-3) or 15 min (MAM-1, MAM-2). Quenching of unreacted MAM solution was carried out by a 10-min incubation with 10 mM *N*-acetyl-L-cysteine methyl ester (Sigma-Aldrich), in ice-cold PBS, pH 8.0. Dishes were rapidly washed with PBS and incubated with a thiol-cleavable, membrane-impermeant reagent sulfosuccinimidyl-2-(biotinamido)ethyl-1, 3-dithiopropionate (Sulfo-NHS-SS-Biotin; ThermoFisher Scientific) in PBS at pH 8.0 for 30 min under gentle agitation. Unreacted Sulfo-NHS-SS-Biotin was quenched by incubation with 20 mM Tris(hydroxymethyl)aminomethane (Biosolve Chemicals) in ice-cold PBS, pH 8.0, for 10 min. Cells were solubilized in lysis buffer, and the supernatant was incubated overnight with neutravidin-agarose beads (ThermoFisher Scientific) as previously described (43). Protein samples were separated on 4–15% SDS/PAGE gels in Tris/Glycine/SDS running buffer (Bio-Rad). Samples were transferred to a nitrocellulose membrane as described (43), which was then incubated in TPBS (PBS supplemented with 1% nonfat dry milk, 0.5% BSA, and 0.05% Tween 20) to block the membrane. The membrane was incubated in TPBS buffer overnight at 4 °C with mouse anti–c-Myc antibody (ThermoFisher Scientific) diluted at 1:2,500. After three washes with TPBS, the blot was incubated with peroxidase-conjugated sheep anti-mouse antibody for 2 h (dilution 1:10,000; GE Healthcare life Sciences) at room temperature and washed a further three times with TPBS and developed using Amersham ECL Prime Western blotting detection reagent (Dominique Dutscher).

Fluorescence Measurements. Fluorescence was measured using an Olympus IX73 (Olympus LUCPlanFLN 20×/0.45 PH1) with ProgRes MF-cool camera. Images were captured at 0.5 Hz. For each experiment, YO-PRO-1 (ThermoFisher) fluorescence was measured from three single cells per field with excitation at 455 nm (ET-EGFP filter, Chroma). For the double-mutant I328C/S345C, cells were first incubated with 10 μM MAM-2 in the presence of 3 μM ATP for 10 min and washed with NES buffer. Then, cells were incubated with 10 μM YO-PRO-1 (4-[(3-methyl-1,3-benzoxazol-2(3H)-ylidene)methyl]-1-[3-(trimethylammonio)propyl]quinolinium diiodide) in NES, and following 10 min of incubation, cells were irradiated at 365 nm for 5 s. For single-mutant I328C and S345C, the same protocol was carried out, except that activation was achieved by 530 nm irradiation and that cells were briefly preirradiated at 365 nm before YO-PRO-1 incubation to reset the azobenzene in the *cis* state. In control experiments with the P2X2–3T, the incorporation of 10 μM YO-PRO-1 was measured in response to 30 μM ATP.

Molecular Modeling. The end-to-end distances for the free MAM-1 and MAM-2 molecules in solution (~10,000 atoms with water molecules) were obtained from all-atom MD simulations performed with ACEMD (44). Eight 100 ns-long unrestrained MD simulations were computed in the NVT ensemble at 310 K for the *cis* and *trans* configurations and for the R/R, S/R, R/S, and S/S stereoisomers. The mean distances between the S–S atoms were computed by averaging over the four stereoisomers for a total of n = 200,000 per *cis* or *trans* configuration. Normalized probability distributions of the S–S distance were obtained by clustering all distance values using a bin width of 0.5 Å. The permeation mechanism of Na^+,

$NMDG^+$, YO-PRO-1^{2+}, and spermidine^{3+} in P2X was explored by all-atom MD simulations starting from a relaxed open-state model of zfP2X4 stabilized by three vertical MAM-2 photo-switchable cross-linkers fused at the positions I336C/N353C in cis configuration. The latter model (~138,000 atoms) was produced following the procedure described previously (36), with a few differences: (*i*) Three MAM-2 (instead of MAM-3) cross-linkers were fused to zfP2X4 with the glycine unit placed downward near N353C; (*ii*) the 2-ns equilibration MD was followed by a production of 50 ns with no positional restraints; (*iii*) in addition to the distance restraints mimicking the internal TM1/TM2 Cd^{2+} binding site (45), the symmetry of the P2X trimer was loosely controlled by using the "Symmetry Restraints" command in NAMD with force constants of 0.25 and 1.0 kcal·mol^{-1}·Å^{-2} for the extracellular and the transmembrane domains, respectively; and (*iv*) the side chain of L351 involved in the new TM2–TM2 interface was simulated using four noninteracting copies (46) together with the R/R, R/S, S/R, and S/S stereoisomers of MAM-2.

For the MD simulations of cation permeation, two modifications were introduced in the resulting model of the P2X open state. First, the MAM-2 linkers were removed (while keeping the mutated residues into cysteines) to mimic the physiological conditions. Second, the extracellular domain of the receptor was deleted to reduce the size of the system and to enhance the sampling of permeation events on the simulation timescale. This modification was done by introducing a peptide bond between D59 and F333 at the top of the transmembrane domain. The resulting structure was energy-minimized for 5,000 steps with NAMD 2.11 (47) using the CHARMM force-field version 36 (48). $NMDG^+$, YO-PRO-1^{2+}, and spermidine^{3+} parameters were obtained from the CHARMM general force field (49). During all simulations, harmonic restraints (5 kcal·mol^{-1}·Å^{-2}) on the backbone atoms of the protein were applied to preserve the configuration of the transmembrane domain as in the MAM2-equilibrated model. The receptor was then embedded into a pre-equilibrated 1-palmitoyl-2-oleoyl-sn-glycero-3-phosphocholine (POPC) lipid bilayer, solvated with TIP3P water molecules and NaCl at 0.15 M or 1 M concentration using VMD (50). To study permeation of large organic cations, Na^+ ions were replaced by $NMDG^+$, YO-PRO-1^{2+}, or spermidine^{3+} (51). All simulations were performed with periodic boundary conditions and Particle Mesh Ewald long-range electrostatics. The system (~90,000 atoms) was minimized during 5,000 steps, briefly thermalized (600ps) to 300K, and equilibrated for 2 ns in the NPT ensemble at 1 atm pressure. Production runs were performed in NVT ensemble imposing a membrane potential to increase the ion permeation probability on the simulation timescale. The membrane potential V_m was generated by introducing a constant electric field E_z on all atoms along the *z* axis perpendicular to the membrane plane (52), $E_z = V_m/L_z$, where L_z is the size of the simulated system in the *z* direction. The membrane potential was set to the following voltages: –2, –1.5, and –1 V. Analysis of ion permeation was done using Tcl scripting in VMD, whereas the pore profiles were computed by the program HOLE (53). The End-to-End distance of permeant $NMDG^+$ was computed at each simulation step as the distance between the two terminal carbons. To compute the horizontality, we selected a vector from the center of mass of the molecule to the terminal carbon linked to the nitrogen, and then the complement of the polar angle was computed. The *z* coordinate of the center of mass of permeant $NMDG^+$ was plotted as a function of the two previous observables.

Data Analysis. All experiments were performed at least four times from at least two transfections, and values are presented as mean ± SEM. For modeling, values of distribution of *cis* and *trans* configurations are presented as mean ± SE. The number of cells or patches used for the experiments is provided in the text or corresponding figure legends.

ACKNOWLEDGMENTS. We thank Professor Hongbo Zhao and Dr. François Rassendren for providing human P2X2 and human P2X3 receptors, respectively; and Dr. Frederic Bolze and Romain Vauchelles for imaging advising. This work was supported by Agence Nationale de la Recherche Grant ANR-14-CE11-0004-01 (to T.G.), the Ministère de la Recherche, and the Fondation Pierre et Jeanne Spiegel. Financial support from the International Center for Frontier Research in Chemistry (icFRC) and the Agence Nationale de la Recherche through the LabEx project Chemistry of Complex Systems (ANR-10-LABX-0026 CSC; to M.C.) is gratefully acknowledged. This work was granted access to the High Performance Computing resources of the Centre de Calcul Recherche et Technologie/Centre Informatique National de l'Enseignement Supérieur/Institut du Développement et des Ressources en Informatique Scientifique under the allocation 2016-[076644] made by the Grand Equipement National de Calcul Intensif.

1. Idzko M, Ferrari D, Eltzschig HK (2014) Nucleotide signalling during inflammation. *Nature* 509:310–317.
2. Khakh BS, North RA (2012) Neuromodulation by extracellular ATP and P2X receptors in the CNS. *Neuron* 76:51–69.
3. Wirkner K, Sperlagh B, Illes P (2007) P2X3 receptor involvement in pain states. *Mol Neurobiol* 36:165–183.
4. Yan D, et al. (2013) Mutation of the ATP-gated P2X(2) receptor leads to progressive hearing loss and increased susceptibility to noise. *Proc Natl Acad Sci USA* 110: 2228–2233.
5. Pijacka W, et al. (2016) Purinergic receptors in the carotid body as a new drug target for controlling hypertension. *Nat Med* 22:1151–1159.
6. North RA, Jarvis MF (2013) P2X receptors as drug targets. *Mol Pharmacol* 83:759–769.
7. Kawate T, Michel JC, Birdsong WT, Gouaux E (2009) Crystal structure of the ATP-gated P2X(4) ion channel in the closed state. *Nature* 460:592–598.
8. Hattori M, Gouaux E (2012) Molecular mechanism of ATP binding and ion channel activation in P2X receptors. *Nature* 485:207–212.
9. Kasuya G, et al. (2016) Structural insights into divalent cation modulations of ATP-gated P2X receptor channels. *Cell Reports* 14:932–944.
10. Mansoor SE, et al. (2016) X-ray structures define human P2X(3) receptor gating cycle and antagonist action. *Nature* 538:66–71.
11. Karasawa A, Kawate T (2016) Structural basis for subtype-specific inhibition of the P2X7 receptor. *eLife* 5:5.
12. Browne LE, Jiang LH, North RA (2010) New structure enlivens interest in P2X receptors. *Trends Pharmacol Sci* 31:229–237.
13. Habermacher C, Dunning K, Chataigneau T, Grutter T (2016) Molecular structure and function of P2X receptors. *Neuropharmacology* 104:18–30.
14. Ding S, Sachs F (1999) Single channel properties of P2X2 purinoceptors. *J Gen Physiol* 113:695–720.
15. Evans RJ (1996) Single channel properties of ATP-gated cation channels (P2X receptors) heterologously expressed in Chinese hamster ovary cells. *Neurosci Lett* 212: 212–214.
16. Riedel T, Schmalzing G, Markwardt F (2007) Influence of extracellular monovalent cations on pore and gating properties of P2X7 receptor-operated single-channel currents. *Biophys J* 93:846–858.
17. Virginio C, MacKenzie A, Rassendren FA, North RA, Surprenant A (1999) Pore dilation of neuronal P2X receptor channels. *Nat Neurosci* 2:315–321.
18. Khakh BS, Bao XR, Labarca C, Lester HA (1999) Neuronal P2X transmitter-gated cation channels change their ion selectivity in seconds. *Nat Neurosci* 2:322–330.
19. Rokic MB, Stojilkovic SS (2013) Two open states of P2X receptor channels. *Front Cell Neurosci* 7:215.
20. Wei L, Caseley E, Li D, Jiang LH (2016) ATP-induced P2X receptor-dependent large pore formation: How much do we know? *Front Pharmacol* 7:5.
21. Compan V, et al. (2012) P2X2 and P2X5 subunits define a new heteromeric receptor with P2X7-like properties. *J Neurosci* 32:4284–4296.
22. Jiang LH, et al. (2005) N-methyl-D-glucamine and propidium dyes utilize different permeation pathways at rat P2X(7) receptors. *Am J Physiol Cell Physiol* 289:C1295–C1302.
23. Pelegrin P, Surprenant A (2006) Pannexin-1 mediates large pore formation and interleukin-1beta release by the ATP-gated P2X7 receptor. *EMBO J* 25:5071–5082.
24. Eickhorst AN, Berson A, Cockayne D, Lester HA, Khakh BS (2002) Control of P2X(2) channel permeability by the cytosolic domain. *J Gen Physiol* 120:119–131.
25. Fisher JA, Girdler G, Khakh BS (2004) Time-resolved measurement of state-specific P2X2 ion channel cytosolic gating motions. *J Neurosci* 24:10475–10487.
26. Khakh BS, Egan TM (2005) Contribution of transmembrane regions to ATP-gated P2X2 channel permeability dynamics. *J Biol Chem* 280:6118–6129.
27. Chaumont S, Khakh BS (2008) Patch-clamp coordinated spectroscopy shows P2X2 receptor permeability dynamics require cytosolic domain rearrangements but not Panx-1 channels. *Proc Natl Acad Sci USA* 105:12063–12068.
28. Yan Z, Li S, Liang Z, Tomić M, Stojilkovic SS (2008) The P2X7 receptor channel pore dilates under physiological ion conditions. *J Gen Physiol* 132:563–573.
29. Shinozaki Y, et al. (2009) Direct observation of ATP-induced conformational changes in single P2X(4) receptors. *PLoS Biol* 7:e1000103.
30. Khadra A, et al. (2012) Gating properties of the P2X2a and P2X2b receptor channels: Experiments and mathematical modeling. *J Gen Physiol* 139:333–348.
31. Browne LE, Compan V, Bragg L, North RA (2013) P2X7 receptor channels allow direct permeation of nanometer-sized dyes. *J Neurosci* 33:3557–3566.
32. Li M, Toombes GE, Silberberg SD, Swartz KJ (2015) Physical basis of apparent pore dilation of ATP-activated P2X receptor channels. *Nat Neurosci* 18:1577–1583.
33. Ding S, Sachs F (1999) Ion permeation and block of P2X(2) purinoceptors: Single channel recordings. *J Membr Biol* 172:215–223.
34. Sorge RE, et al. (2012) Genetically determined P2X7 receptor pore formation regulates variability in chronic pain sensitivity. *Nat Med* 18:595–599.
35. Li M, Chang TH, Silberberg SD, Swartz KJ (2008) Gating the pore of P2X receptor channels. *Nat Neurosci* 11:883–887.
36. Habermacher C, et al. (2016) Photo-switchable tweezers illuminate pore-opening motions of an ATP-gated P2X ion channel. *eLife* 5:e11050.
37. Browne LE, et al. (2014) Optical control of trimeric P2X receptors and acid-sensing ion channels. *Proc Natl Acad Sci USA* 111:521–526.
38. Guerra GP, Rubin MA, Mello CF (2016) Modulation of learning and memory by natural polyamines. *Pharmacol Res* 112:99–118.
39. Pippel A, et al. (2017) Localization of the gate and selectivity filter of the full-length P2X7 receptor. *Proc Natl Acad Sci USA* 114:E2156–E2165.
40. Clyne JD, Brown TC, Hume RI (2003) Expression level dependent changes in the properties of P2X2 receptors. *Neuropharmacology* 44:403–412.

41. Fujiwara Y, Kubo Y (2004) Density-dependent changes of the pore properties of the P2X2 receptor channel. *J Physiol* 558:31–43.
42. Tochitsky I, et al. (2016) How azobenzene photoswitches restore visual responses to the blind retina. *Neuron* 92:100–113.
43. Jiang R, et al. (2010) A putative extracellular salt bridge at the subunit interface contributes to the ion channel function of the ATP-gated P2X2 receptor. *J Biol Chem* 285:15805–15815.
44. Harvey MJ, Giupponi G, Fabritiis GD (2009) ACEMD: Accelerating biomolecular dynamics in the microsecond time scale. *J Chem Theory Comput* 5: 1632–1639.
45. Heymann G, et al. (2013) Inter- and intrasubunit interactions between transmembrane helices in the open state of P2X receptor channels. *Proc Natl Acad Sci USA* 110:E4045–E4054.
46. Roitberg A, Elber R (1991) Modeling side chains in peptides and proteins: Application of locally enhanced sampling and simulated annealing methods to find minimum energy conformations. *J Chem Phys* 95:9277–9287.
47. Phillips JC, et al. (2005) Scalable molecular dynamics with NAMD. *J Comput Chem* 26: 1781–1802.
48. Best RB, et al. (2012) Optimization of the additive CHARMM all-atom protein force field targeting improved sampling of the backbone φ, ψ and side-chain χ(1) and χ(2) dihedral angles. *J Chem Theory Comput* 8:3257–3273.
49. Vanommeslaeghe K, et al. (2010) CHARMM general force field: A force field for drug-like molecules compatible with the CHARMM all-atom additive biological force fields. *J Comput Chem* 31:671–690.
50. Humphrey W, Dalke A, Schulten K (1996) VMD: Visual molecular dynamics. *J Mol Graph* 14:27–38.
51. Onasch F, et al. (1984) The interactions between nucleic acids and polyamines. III. Microscopic protonation constants of spermidine. *Biophys Chem* 19:245–253.
52. Roux B (2008) The membrane potential and its representation by a constant electric field in computer simulations. *Biophys J* 95:4205–4216.
53. Smart OS, Neduvelil JG, Wang X, Wallace BA, Sansom MS (1996) HOLE: A program for the analysis of the pore dimensions of ion channel structural models. *J Mol Graph* 14:354–360, 376.